nature neuroscience

Supplementary information

https://doi.org/10.1038/s41593-026-02279-z

Brain motion is driven by mechanical coupling with the abdomen

In the format provided by the authors and unedited

Supplementary material for:
"Brain motion is driven by mechanical coupling with the abdomen", Garborg et al.

Supplementary Table 1. Simulation geometry data and constitutive parameters. Dimensions of the central sinus compartment adopted in this geometry (i.e., R_{cs} and L_{cs}) were chosen to match the reference volume of a cylindrical central sinus with radius and length of $150\ \mu\mathrm{m}$ and $15\ \mathrm{mm}$, respectively.

Geometric parameter	**Symbol**	**Value [units] or Definition**
Radius of cerebrum (brain)	R_{b}	$5\ \mathrm{mm}$
Radius of spherical ventricle	R_{v}	$0.5\ \mathrm{mm}$
Radius of central canal	R_{cc}	$40\ \mu\mathrm{m}$
Radius of spinal cord	R_{sc}	$1.25\ \mathrm{mm}$
Thickness of meningeal layer	t_{m}	$20\ \mu\mathrm{m}$
Radius of central sinus	R_{cs}	$0.35\ \mathrm{mm}$
Length of spinal cord	L_{sc}	$50\ \mathrm{mm}$
Length of central sinus	L_{cs}	$2.7551\ \mathrm{mm}$
Length of squeeze zone	L_{sz}	$20\ \mathrm{mm}\ (= 40\%L_{\mathrm{sc}})$
z-coord. of $P_{\mathrm{sz},1}$	$z_{P_{\mathrm{sz},1}}$	$-55\%(R_{\mathrm{b}} + L_{\mathrm{sc}})$
z-coord. of $P_{\mathrm{sz},2}$	$z_{P_{\mathrm{sz},2}}$	$-95\%(R_{\mathrm{b}} + L_{\mathrm{sc}})$
Constitutive/material parameter	**Symbol**	**Value [units] or Definition**
Fluid true density	ρ_{f}^{*}	$1000\ \mathrm{kg/m^3}$
Solid true density	ρ_{s}^{*}	$1000\ \mathrm{kg/m^3}$
Fluid volume fraction in Ω_{BR}	$\phi_{\mathrm{R,f}}^{\mathrm{BR}}$	0.2
Fluid volume fraction in Ω_{SAS}	$\phi_{\mathrm{R,f}}^{\mathrm{SAS}}$	0.8
Fluid dynamic viscosity	μ_{f}	$0.001\ \mathrm{Pa \cdot s}$
Solid elastic shear modulus in Ω_{BR}	$\mu_{\mathrm{s}}^{\mathrm{e,BR}}$	$2\ \mathrm{kPa}$
Solid elastic shear modulus in Ω_{SAS}	$\mu_{\mathrm{s}}^{\mathrm{e,SAS}}$	$100\ \mathrm{Pa}$
Fluid permeability in Ω_{BR}	$\kappa_{\mathrm{s}}^{\mathrm{BR}}$	$2 \times 10^{-17}\ \mathrm{m^2}$
Fluid permeability in Ω_{SAS}	$\kappa_{\mathrm{s}}^{\mathrm{SAS}}$	$2 \times 10^{-14}\ \mathrm{m^2}$
Resistance coefficient over Γ_{CS}	$\mathrm{res}_{\mathrm{cs}}$	$\alpha_{\mathrm{cs}}\left(\frac{\mu_{\mathrm{f}}}{R_{\mathrm{cs}}}\right)\ \mathrm{Pa \cdot s/m}$
Resistance coefficient over Γ_{out}	$\mathrm{res}_{\mathrm{out}}$	$\alpha_{\mathrm{out}}\left(\frac{\mu_{\mathrm{f}}}{t_{\mathrm{m}}}\right)\ \mathrm{Pa \cdot s/m}$
Scaling factor for $\mathrm{res}_{\mathrm{cs}}$	α_{cs}	$[10^6, 10^8, 10^8]$
Scaling factor for $\mathrm{res}_{\mathrm{out}}$	α_{out}	$6 \times [10^8, 10^6, 10^8]$

Interface viscosity parameter on Γ	μ_S	1×10^6Pa·s/m

Supplementary Material — Finite Element Formulation and Boundary Conditions

Notation

Here we report the weak form of the governing equations. To avoid proliferation of symbols, given a field ζ, the test function for that field will be denoted by $\tilde{\zeta}$. We denote the reference configuration of the solid phase by Ω_s. We recall that we have assumed Ω_s to coincide with Ω, the initial configuration of the mixture. We formulate the weak form of our problem over Ω_s. As noted in the main text, $\Omega_{\mathrm{BR}}(t)$ and $\Omega_{\mathrm{SAS}}(t)$ are time dependent domains. We denote by $\boldsymbol{X}_\mathrm{s}$ points in Ω_s. Denoting the motion of the solid by $\boldsymbol{\chi}_\mathrm{s}(\boldsymbol{X}_\mathrm{s}, t)$, under common assumptions from mixture theory, $\boldsymbol{\chi}_\mathrm{s}$ is a smooth map with smooth inverse from Ω_s to $\Omega(t)$ (cf. [1-4]). The gradients over $\Omega(t)$ and $\Omega_\mathrm{s}$will be denoted by ∇ and ∇_s, respectively. Given a quantity $\zeta(\boldsymbol{x}, t)$ over $\Omega(t)$, ζ^σ is defined as $\zeta^\sigma(\boldsymbol{X}_\mathrm{s}, t) = \zeta(\boldsymbol{\chi}_\mathrm{s}(\boldsymbol{X}_\mathrm{s}, t), t)$. In view of our assumptions, Ω_{BR} and Ω_{SAS} happen to be the inverse images of $\Omega_{\mathrm{BR}}(t)$ and $\Omega_{\mathrm{SAS}}(t)$, under $\boldsymbol{\chi}_\mathrm{s}$, respectively. The fields $\boldsymbol{u}_\mathrm{s}$, $\mathbf{F}_\mathrm{s}$, and $J_\mathrm{s}$are understood to have Ω_s as their domain. Given any two fields ζ and φ over some domain Θ such that their (pointwise) inner-product is meaningful, we denote by $(\zeta, \varphi)_\Theta$ the integral over Θ of said inner product. We denote by Γ, the inverse image of the brain-SAS interface under the solid phase motion. The notation $(\llbracket \zeta, \varphi \rrbracket)_\Gamma$ will indicate the integral over Γ of the jump of the inner-product of ζ and φ across Γ.

Weak Form

Referring to Fig. 6a, for ease of writing, the weak form shown here is written assuming that $\boldsymbol{u}_\mathrm{s}$ and $\boldsymbol{v}_\mathrm{f}^\sigma$ are prescribed on $\partial\Omega_\mathrm{s}^{\mathrm{ext}} = \Gamma_{\mathrm{ext}} \cup \Gamma_{\mathrm{out}} \cup \Gamma_{\mathrm{SZ}}$. The detailed specification of the boundary conditions is then provided in the next subsection. The weak form is as follows:

$$
\begin{aligned}
&(\tilde{\boldsymbol{u}}_\mathrm{s}, J_s(\rho_s \boldsymbol{a}_\mathrm{s} + \rho_\mathrm{f}\boldsymbol{a}_\mathrm{f} - \boldsymbol{b}_\mathrm{s} - \boldsymbol{b}_\mathrm{f})^\sigma)_{\Omega_\mathrm{s}} \\
&\quad + \left(\nabla\tilde{\boldsymbol{u}}_\mathrm{s}, J_\mathrm{s}(\mathbf{T}_\mathrm{s}^e + \mathbf{T}_\mathrm{s}^v + \mathbf{T}_\mathrm{f}^v)^\sigma\, \mathbf{F}_\mathrm{s}^{-\mathrm{T}}\right)_{\Omega_\mathrm{s}} \\
&\quad + \Big((\tilde{\boldsymbol{v}}_\mathrm{f})^\sigma, J_s\Big(\rho_\mathrm{f}\boldsymbol{a}_\mathrm{f} - \boldsymbol{b}_\mathrm{f} + \phi_\mathrm{f}\nabla p \\
&\quad + (\mu_D\, \phi_\mathrm{f}^2/\kappa_\mathrm{s})(\boldsymbol{v}_\mathrm{f} - \boldsymbol{v}_\mathrm{s})\Big)^\sigma\Big)_{\Omega_\mathrm{s}} \\
&\quad + \left(\tilde{\boldsymbol{u}}_\mathrm{s}, \llbracket \rho_\mathrm{f}(\boldsymbol{v}_\mathrm{f} - \boldsymbol{v}_\mathrm{s}) \otimes (\boldsymbol{v}_\mathrm{f} - \boldsymbol{v}_\mathrm{s}) + p\mathbf{I}\rrbracket^\sigma J_\mathrm{s}\mathbf{F}_\mathrm{s}^{-\mathrm{T}}\boldsymbol{m}_\mathrm{s}\right)_\Gamma \\
&\quad - \left(\llbracket(\tilde{\boldsymbol{v}}_\mathrm{f})^\sigma, \left(k_\mathrm{f}\mathbf{I} - \rho_\mathrm{f}\boldsymbol{v}_\mathrm{f} \otimes (\boldsymbol{v}_\mathrm{f} - \boldsymbol{v}_\mathrm{s})\right)^\sigma J_\mathrm{s}\mathbf{F}_\mathrm{s}^{-\mathrm{T}}\boldsymbol{m}_\mathrm{s}\rrbracket\right)_\Gamma \\
&\quad - \Big(\Big\llbracket(\tilde{\boldsymbol{v}}_\mathrm{f})^\sigma, \Big(\phi_\mathrm{f}(\wp - p)\mathbf{I} - \tfrac{1}{2}\phi_\mathrm{f}\mu_S\llbracket\boldsymbol{v}_\mathrm{flt}\rrbracket \\
&\quad \otimes \boldsymbol{m}\Big)^\sigma\Big\rrbracket J_\mathrm{s}\mathbf{F}_\mathrm{s}^{-\mathrm{T}}m_\mathrm{s}\Big)_\Gamma - \left(\mathbf{F}_\mathrm{s}^{-\mathrm{T}}(\nabla\tilde{p})^\sigma, J_\mathrm{s}(\boldsymbol{v}_\mathrm{s} + \boldsymbol{v}_\mathrm{flt})^\sigma\right)_{\Omega_\mathrm{s}} \\
&\quad - \left(\llbracket(\tilde{p})^\sigma J_\mathrm{s}\mathbf{F}_\mathrm{s}^{-\mathrm{T}}\boldsymbol{m}_\mathrm{s}, (\boldsymbol{v}_\mathrm{s} + \boldsymbol{v}_\mathrm{flt})^\sigma\rrbracket\right)_\Gamma \\
&\quad + \left((\tilde{\wp})^\sigma, \llbracket\boldsymbol{v}_\mathrm{flt}\rrbracket^\sigma \cdot J_\mathrm{s}\mathbf{F}_\mathrm{s}^{-\mathrm{T}}\boldsymbol{m}_\mathrm{s}\right)_\Gamma \\
&\quad + \left((\tilde{p})^\sigma J_\mathrm{s}\mathbf{F}_\mathrm{s}^{-\mathrm{T}}\boldsymbol{n}_\mathrm{s}, (\boldsymbol{v}_\mathrm{s} + \boldsymbol{v}_\mathrm{flt})^\sigma\right)_{\partial\Omega_\mathrm{s}^{\mathrm{ext}}} = 0,
\end{aligned}
\tag{10}
$$

where $\partial\Omega_{\mathrm{s}}^{\mathrm{ext}}$ denotes the outer-most boundary of Ω_s , as defined above, and $\boldsymbol{n}_{\mathrm{s}}$ is the associated outward unit normal. The above weak form, modified to enforce the boundary conditions listed later, is required to hold for all test functions $\tilde{\boldsymbol{u}}_{\mathrm{s}}$, $\tilde{\boldsymbol{v}}_{\mathrm{f}}$, $\tilde{p}$, and $\tilde{\wp}$ in functional spaces chosen in a coordinated manner to the functional spaces selected for the unknown fields $\boldsymbol{u}_{\mathrm{s}}$, $\boldsymbol{v}_{\mathrm{f}}$, p, and $\wp$. As a formal analysis concerning the well-posedness of the problem considered in this paper has yet to be developed, we avoid characterizing the spaces in question using the formal language of Sobolev spaces. Rather, we limit ourselves to describing the details of our practical implementation. With the few exceptions that we will describe next, our implementation follows standard practices in the FEM literature on solid and fluid mechanics (cf. [5]).

As mentioned in the main body of the paper, $\boldsymbol{u}_{\mathrm{s}}$ is globally continuous over Ω_{s}. Its numerical representation was done using a second-order Lagrange polynomial FE field. The fields $\boldsymbol{v}_{\mathrm{f}}^{\sigma}$ and p^{σ} were taken to be continuous over the subsets of Ω_{s} corresponding to $\Omega_{\mathrm{BR}}^{\sigma}$ and $\Omega_{\mathrm{SAS}}^{\sigma}$. However, these fields are not continuous across Γ. The FE fields taken to interpolate $\boldsymbol{v}_{\mathrm{f}}$ and p were second-order and first-order Lagrange polynomials, respectively. The field $\wp$ was taken to be continuous over Γ (this field does not exist away from Γ) and interpolated using first-order Lagrange polynomials.

Note on Integration by Parts

The weak enforcement of Eq. (1), namely the continuity equation for this problem, was done by testing said equation by $\tilde{p}$, integrating the resulting form over the problem's domain, and applying integration by parts. This treatment of the continuity equation is not standard. The rationale for this approach is the desire to avoid approximating the gradient of the volume fraction ϕ_f. This choice has additional consequences in the treatment of the momentum equations and any boundary condition involving boundary tractions. In the momentum equations, we do *not* apply integration by parts to terms involving the gradient of the pore pressure. When it comes to boundary tractions, as it would be physically incorrect to prescribe pore pressure boundary values, we retain the associated pore pressure in the boundary contributions.

Note on Implementation of Boundary Conditions Involving Traction

Here we indicate boundary conditions involving tractions in the *current configuration* of the system. This is done to facilitate the readability. As indicated earlier, the motion of the solid phase provides the ALE map needed for the pullback of said conditions to the actual computational domain. This said, we note that our computations were carried out using COMSOL Multiphysics® (v. 6.2. www.comsol.com. COMSOL AB, Stockholm, Sweden). The latter provides automatic support for these operations. That is, a user can specify whether a

contribution to a weak form is to be evaluated in the "Spatial" frame (here $\Omega(t)$) or the "Material" frame (here Ω_s). We have taken advantage of this feature in our calculations.

Boundary Conditions

With reference to Fig. 6, the overall geometry of the system is axially symmetric and a cylindrical coordinate system is defined such that the z axis is the dashed line in the figure with the positive direction from the tail towards the head. The radial coordinate r is in the direction perpendicular to the z axis. By $\boldsymbol{e}_r$ we denote the unit vector in the radial direction. The boundary of the brain-SAS over which boundary conditions are applied consists of the surface Γ_{CS} surrounding the central sinus, and of the union of the subsets Γ_{out}, Γ_{ext}, and Γ_{SZ}. Γ_{out} is an outlet /inlet meant to represent a structure like the cribriform plate through which CSF can exit/enter the system. Γ_{SZ} is the region on which the squeezing action of the VVP onto the dural sack is applied. Γ_{ext} denotes the remaining portion of the SAS external boundary. Our simulations were 2D axisymmetric. Axial symmetry was enforced in a standard fashion, namely requiring the radial component of vector fields vanish at the z-axis. The rest of the boundary conditions are as follows:

- $\boldsymbol{u}_{\mathrm{s}} = \boldsymbol{0}$ on $\Gamma_{\mathrm{ext}} \cup \Gamma_{\mathrm{out}}$.
- $\boldsymbol{u}_{\mathrm{s}} = -u_{0,\mathrm{rad}}(t) f_{\mathrm{SZ,space}}(z)\boldsymbol{e}_r$ on Γ_{SZ}, where
    - $f_{\mathrm{SZ,space}}(z)$ is a (unit) step function over the spatial interval $z_{P_{\mathrm{SZ},2}} < z < z_{P_{\mathrm{SZ},1}}$ smoothed so to be continuous up to 2nd order derivatives over transition zones with $z_{P_{\mathrm{SZ},2}} < z < z_{P_{\mathrm{SZ},2}} + 0.1(z_{P_{\mathrm{SZ},1}} - z_{P_{\mathrm{SZ},2}})$ and $z_{P_{\mathrm{SZ},1}} - 0.1(z_{P_{\mathrm{SZ},1}} - z_{P_{\mathrm{SZ},2}}) < z < z_{P_{\mathrm{SZ},1}}$.
    - $u_{o,\mathrm{rad}}$ is a positive scalar function of time subject to the following constraint: $\frac{1}{|\Gamma_{\mathrm{SZ}}(t)|}\int_{\Gamma_{\mathrm{SZ(t)}}} \boldsymbol{n}\cdot\mathbf{T}\boldsymbol{n}\,d\Gamma = -p_0 f_{\mathrm{SZ,time}}(t)$, where $\mathbf{T}$ is the total Cauchy stress acting on the mixture (i.e., solid and fluid phases combined), $\boldsymbol{n}$ is the outward unit normal in the current configuration on $\Gamma_{\mathrm{SZ}}(t)$, p_0 a prescribed pressure value, and $f_{\mathrm{SZ,time}}(t)$ a unit step function over the time interval $0 < t < t_{\mathrm{squeeze}}$, smoothed so to be continuous up to 2nd order derivatives over a transition zones 10% in size of the function's support. That is, $u_{o,\mathrm{rad}}(t)$ was controlled so that the spatial average of the normal traction over the SZ was equivalent to a uniform pressure distribution of value p_0.
- $\boldsymbol{v}_{\mathrm{f}} = \boldsymbol{v}_{\mathrm{s}}$ on $\Gamma_{\mathrm{ext}} \cup \Gamma_{\mathrm{SZ}} \cup \Gamma_{\mathrm{CS}}$ — This is a "no slip" boundary condition for the fluid relative to solid phase. This boundary condition has been enforced weakly (cf., e.g., [6]).
- Resistance boundary condition on $\Gamma_{\mathrm{CS}}(t)$ — This boundary condition is meant to allow the central sinus (CS) to deform in response to intracranial pressure changes as well as

brain movement. Physiologically, this response is mediated by blood flow in the CS. We have modeled this response through a traction distribution on $\Gamma_{\mathrm{CS}}(t)$ proportional to the velocity of $\Gamma_{\mathrm{CS}}(t)$: $\mathbf{T}\boldsymbol{n} = -\mathrm{res}_{\mathrm{cs}}\boldsymbol{v}_{\mathrm{s}}$, where, again, $\mathbf{T}$ is the total Cauchy stress on the mixture, $\boldsymbol{n}$ is the outward unit normal, and where $\mathrm{res}_{\mathrm{cs}}$ is a resistance constant indicated in Table 1. We have investigated the effects of a range of values of this constant. The boundary condition described here might be viewed as contradicting the condition expressed at the preceding point. However, the boundary conditions in question are both needed, and they are compatible with one another in view of the fact that $\Gamma_{\mathrm{CS}}(t)$ is a moving surface. Hence, the no-slip boundary condition at the previous point pertains the motion of the fluid relative to that of the solid phase, whereas the boundary condition just discussed is meant to characterize, if in a simple manner, how the $\Gamma_{\mathrm{CS}}(t)$ would move in response to changes of blood volume in the central sinus.

- Robin boundary condition on $\Gamma_{\mathrm{out}}(t)$: This is a boundary condition meant to model the outflow of CSF from the skull through pathways like the cribriform plate and the olfactory nerves. In our simulations we have not included sources of production of CSF. Hence, the condition on $\Gamma_{\mathrm{out}}(t)$ is bidirectional, i.e., it allows for both outflow and inflow of CSF. This condition amounts to a hydraulic resistance, which we have implemented as a Robin boundary condition. Specifically, we have enforced the following condition on $\Gamma_{\mathrm{out}}(t)$: $\mathbf{T}_{\mathrm{f}}\boldsymbol{n} = -\mathrm{res}_{\mathrm{out}}\boldsymbol{v}_{\mathrm{flt}}$, where $\mathbf{T}_{\mathrm{f}}$ is the total Cauchy stress on the fluid phase, $\boldsymbol{n}$ is outward unit normal, and $\mathrm{res}_{\mathrm{out}}$ is a constant hydraulic resistance indicated in Table 1. As for $\mathrm{res}_{\mathrm{cs}}$, we have investigated the effects of different values of this constant.

Note on the fluid no-slip boundary condition on Γ_{CS}

In our model, the central sinus is a compliant region bounded by the moving surface Γ_{CS}. The motion of this region is meant to account for some of the vascular response of the bridging veins without an explicit mathematical model of these veins and of the blood flow within them. While our model is very simple, it does ensure that there is no mixing between CSF/ISF and blood that would be present in the central sinus. This constraint is imposed via the no-slip boundary condition over Γ_{CS}. That is, the no-slip condition in question is meant to ensure that no fluid from the poroelastic domain enters or exits the central sinus. As we enforce the no-slip condition weakly, and as there is always an inherent error in numerical computing, we begin with defining some appropriate error indicators meant to substantiate the claim that (within a certain numerical error) there is no fluid flow through Γ_{CS}. Because Γ_{CS} is moving with the solid phase, the no-slip boundary condition in question does not imply that the fluid velocity vanishes over Γ_{CS}; rather it implies that the velocity of the fluid phase is equal to the velocity of solid phase, or, equivalently, that the velocity of the fluid relative to the solid vanishes on Γ_{CS}, or, again

equivalently, when the porosity is not equal to zero, that the filtration velocity vanishes on Γ_{CS}. Therefore, appropriate error norms to assess the effectiveness of our no-slip condition implementation are the $L^2(\Gamma_{\mathrm{CS}})$-norms of the quantities $\boldsymbol{v}_{\mathrm{f}} - \boldsymbol{v}_{\mathrm{s}}$ and $\boldsymbol{v}_{\mathrm{flt}}$, which we denote by $e_{\mathrm{f-s}}$ and e_{flt}, respectively, and we defined them as follows:

$$e_{\mathrm{f-s}} = \left\{ \int_{\Gamma_{\mathrm{cs}}} (\boldsymbol{v}_{\mathrm{f}} - \boldsymbol{v}_{\mathrm{s}}) \cdot (\boldsymbol{v}_{\mathrm{f}} - \boldsymbol{v}_{\mathrm{s}}) \, d\Gamma \right\}^{1/2} \quad \text{and} \quad e_{\mathrm{flt}} = \left\{ \int_{\Gamma_{\mathrm{cs}}} \boldsymbol{v}_{\mathrm{flt}} \cdot \boldsymbol{v}_{\mathrm{flt}} \, d\Gamma \right\}^{1/2}.$$

We now observe that $e_{\mathrm{f-s}}$ and e_{flt} are absolute error measures and that they cannot be divided by the norm of the expected exact results to deduce a corresponding relative error because the expected exact result is equal to zero. Hence, the question arises as to whether they are small or large in relation to the claims we make in the paper. Given that the most prominent claim pertaining to our calculations concerns the fluid flux across the permeable interface Γ, we also introduce the following additional error measure on Γ_{CS}:

$$e_{Q_{\mathrm{CS}}} = \int_{\Gamma_{\mathrm{cs}}} \left| v_{flt} \cdot n_{\mathrm{CS}} \right| d\Gamma,$$

which is the $L^1(\Gamma_{\mathrm{CS}})$ -norm of the normal component of the filtration velocity over Γ_{CS}, i.e., the norm of the fluid flux across Γ_{CS}. We now observe that $e_{Q_{\mathrm{CS}}}$ has the same dimensions of a volumetric flux and it can be directly compared to the flux estimates reported in Fig. 6e thereby providing a practical way to decide if the error in enforcing the no-slip condition on Γ_{CS} is acceptable. For the calculation producing the results in Fig. 6, the error measured defined above are reported in Supplementary Fig.22 as a function of time. In Supplementary Fig. 22a, we report $e_{\mathrm{f-s}}$ and e_{flt}. In Supplementary Fig. 22b, we report $e_{Q_{\mathrm{CS}}}$, along with the plots of Q_{flt} on Γ_{V} and on Γ_{CC} taken from Fig. 6e. The fluxes across Γ_{V} and on Γ_{CC} are so small that they appear as being practically equal to zero when compared to the fluxes across Γ_{SC} and Γ_{BR}. On the plot in Supplementary Fig. 22b, there is a dashed line corresponding to the value of 0.000332 nl/s, which provides an (uniform) upper bound for $e_{Q_{\mathrm{CS}}}$. This upper bound is more than 10^5 smaller than the peak value of Q_{flt}on Γ_{SC} and it is more than 10 times smaller than the peak value of Q_{flt} across Γ_{V}, the latter being the smallest of the fluxes induced by the squeeze on the spinal cord.

Note on Computer Implementation

The mesh and solver were developed using the standard facilities available in COMSOLMultiphysics®. We have employed a mesh consisting of 63204 triangles and 53792 quadrilaterals for a total of 116996 elements. Eight boundary layers with a stretching factor of 1.2 have been placed along the brain-SAS interface. The total number of degrees of freedom is 1,487,531: 690110 for $\boldsymbol{u}_{\mathrm{s}}$, 446546 and 257014 for $\boldsymbol{v}_{\mathrm{f}}$ in the brain and SAS, respectively, 56681 and 33816 for p in the brain and SAS, respectively, 3363 for $\wp$. Finally, there is one degree of freedom for $u_{o,\mathrm{rad}}$. Time integration was carried out using a variable step generalized-α method

[7,8] (this is a 2nd-order method) with a maximum time step set to $0.001s$. The maximum time used for the computations was $10s$, to simulate the $2s$ −squeeze pulse along with the recovery phase of the system after the squeeze ends. The solver was fully coupled and monolithic. MUMPS was selected as the algebraic solver.

Mesh Sensitivity Analysis

The entire poroelastic domain, i.e., the union of the brain and SAS, supports a globally continuous displacement function. To guarantee this property, we used a single conformal mesh covering the entirety of the poroelastic domain. At the same time, the properties of brain and SAS domains are discontinuous. We have ensured this feature by partitioning the mesh so that the elements covering the SAS only share a boundary with nearby elements covering the brain. As a consequence, the element size distribution in our mesh is strongly dominated by the element size of the mesh elements in the SAS, with the added requirement that we chose to have the mesh over the SAS to be more than one element thick. From a modeling perspective our focus was to capture the fluid exchange at the interface between brain and SAS. For this reason, we created a mesh that is locally refined near said interface as opposed to being globally refined. Our mesh was created directly in COMSOL Multiphysics®. It was (i) generated using triangles such that the SAS was, by and large, occupied by a single element in the radial direction, and (ii) refined using a meshing technique called *boundary layers* whereby there is an equal number of layers across the interface in question and such that the layers steadily increase in thickness. We used 8 such layers (on each side of the interface) with a growth ration of 1.2. The resulting number of degrees of freedom has been indicated in the previous section. The mesh is so dense, especially near the SAS-brain interface, that it is not practical to display it for the entire domain in a figure. To ascertain that this mesh was adequate for our needs we proceeded to a mesh sensitivity analysis. First, we meshed the entirety of the domain using quadrilaterals such that the SAS was only one element thick. Then, we partitioned the quadrilaterals into triangles by subdividing them along a diagonal but maintaining the thickness of the SAS to one element. We will refer to this mesh as Mesh 1. As the number of degrees of freedom (DOFs) of Mesh 1 was 588,970, a sensitivity analysis under uniform refinement would have been unfeasible, at least in relation to our current computing resources. We instead proceeded as follows. We created a sequence of three additional meshes, here referred to as Mesh 2, Mesh 3, and Mesh 4, with 2, 4, and 8 boundary layers, respectively. As the initial element through the thickness of the SAS is modified but not removed by the addition of the mesh boundary layers, the total number of elements through the SAS thickness is then 1, 3, 5, and 9 for Meshes 1 to 4. The mesh we used in our study will be referred to as Mesh 5. While this mesh does have 8 boundary layers it was created starting directly from a domain partition

using triangles and therefore it is somewhat different from Mesh 4. Finally, we created an additional mesh, called Mesh 6, obtained from Mesh 1 through a single uniform refinement. The number of degrees of freedom for the meshes is reported in Supplementary Table 2.

	Mesh 1	Mesh 2	Mesh 3	Mesh 4	Mesh 5	Mesh 6
DOFs	588,970	817,894	1,046,818	1,503,816	1,487,531	2,281,026
Relative Error (%)		5.9479e+1	1.3351e-1	2.1432e-2	1.2213e-1	3.9217e+1

Supplementary Table 2. Number of DOFs and estimated percentage relative errors for the results obtained from Meshes 1 through 6.

Again, being our interest focused on exchange rates, we selected the exchange flow rate across Γ_{SC} (cf. Fig. 6e) as the quantity to evaluate for the purpose of our mesh sensitivity analysis. With reference to Fig. 6e, we note that the peak flow rate is achieved slightly before 0.2s from the beginning of the computation. We then proceeded by repeating the computation reported in Fig. 6 for all the meshes mentioned here and over a time interval from 0 to 0.2 seconds. The output of these calculations consists of flow rate values at each reported time step (i.e., every 0.001 second). The computed flow rates are depicted in Supplementary Fig. 20. Visually, the resulting curves become progressively more difficult to distinguish as refinement increases. To obtain a quantitative relative error measure (in the absence of an exact solution), we considered the lists of flow rate values obtained by using each mesh. We will denote by ℓ_i the value list obtained from the calculation based on Mesh *i*. We then computed the following sequence of percentage relative errors: $e_{i+1} = 100\ \|\ell_{i+1} - \ell_i\|/\|\ell_{i+1}\|$, where the list norm is merely the square root of the sum of the squares of the entries of the list, each list having 201 entries. Using Mesh 4 as a reference we see that Mesh 6 has a worse performance than Mesh 5, confirming that in this computation one can limit refinement near the brain-SAS interface. Furthermore, we see that Mesh 5 yields a small relative error with respect to Mesh 4. So, in the end, we chose Mesh 5 for our calculations as it consisted of fewer DOFs than Mesh 4 while still providing an acceptable level of accuracy. Another reason for choosing this mesh is that we found that the performance of a mesh is not uniform across all the parameter values we have used to produce the results in this paper. Mesh 5 is the mesh that we felt gave acceptable results across all cases. We have computed the relative errors using a Python script (called mesh_study.py), which we included in the Supplementary Materials. All the meshes used in this study have been made available within a COMSOL Multiphysics® file called main_test_MeshStudy.mph as well as standalone Nastran files called Meshx.nas, with x going from 1 to 6.

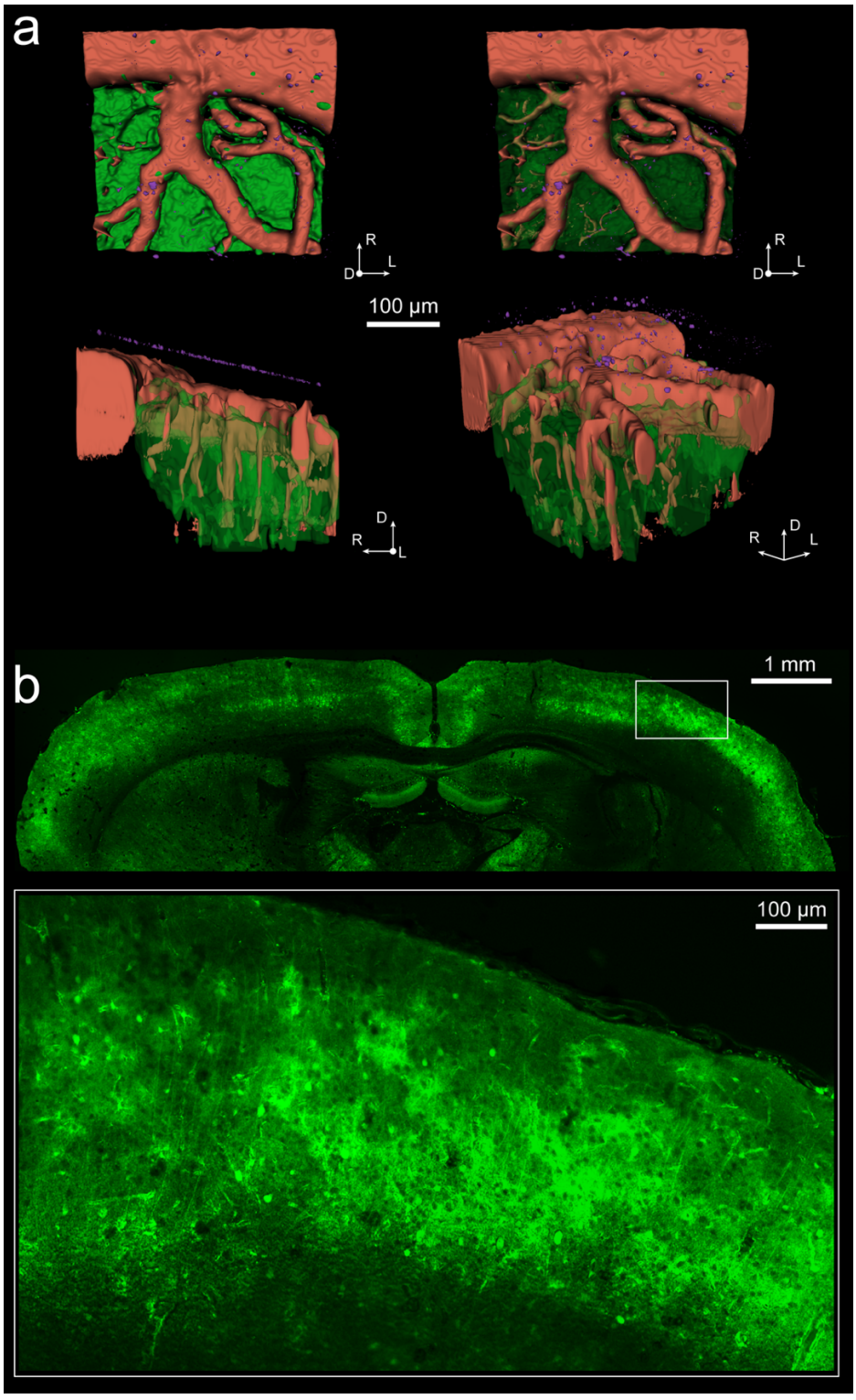

Supplementary Figure 1. Microspheres and brain. a. Reconstruction of GFP-expressing parenchyma (green), blood vessels (red), and fluorescent microspheres (magenta). The axes are labeled dorsal (D), rostral (R), and lateral (L). Penetrating vessels can be seen through the semi-transparent brain in the bottom left and bottom right images. **b.** Coronal section of a GFP-expressing mouse brain, showing ubiquitous labeling of cells.

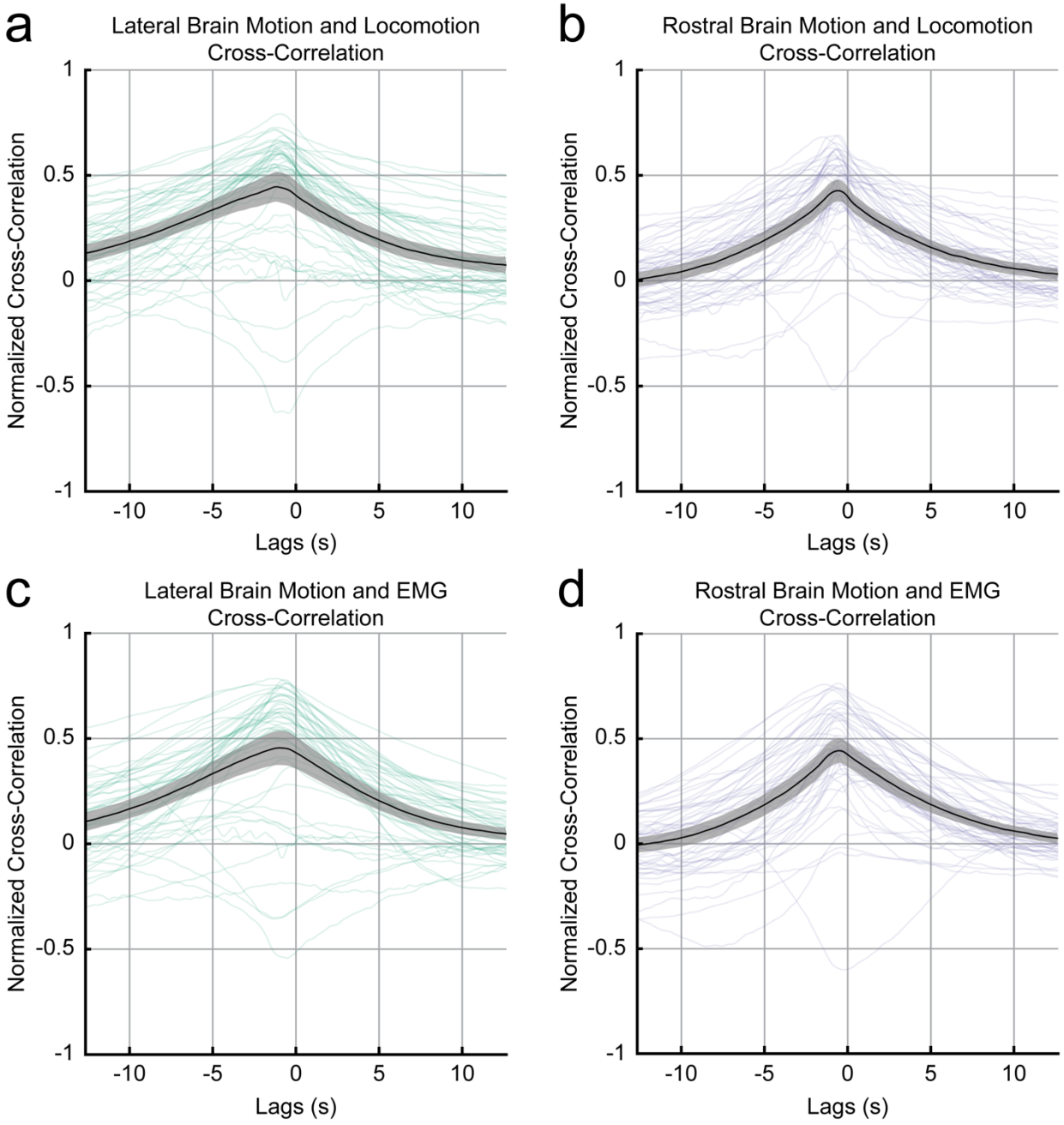

Supplementary Figure 2. Cross-correlations between cortical brain motion, locomotion and abdominal EMG. a. Cross-correlation between locomotion and lateral cortical motion. Negative lags indicate locomotion leads brain motion. Black line shows mean, with shading showing 90 percent confidence interval. N = 153 locomotion events. **b.** Cross-correlation between locomotion and rostral cortical motion. Negative lags indicate locomotion leads brain motion. Black line shows mean, with shading showing 90 percent confidence interval. N = 153 locomotion events. **c.** Cross-correlation between EMG and lateral cortical motion. Negative lags indicate EMG leads brain motion. Black line shows mean, with shading showing 90 percent confidence interval. N = 108 EMG events. **d.** Cross-correlation between EMG and rostral cortical motion. Negative lags indicate EMG leads brain motion. Black line shows mean, with shading showing 90 percent confidence interval. N = 108 EMG events.

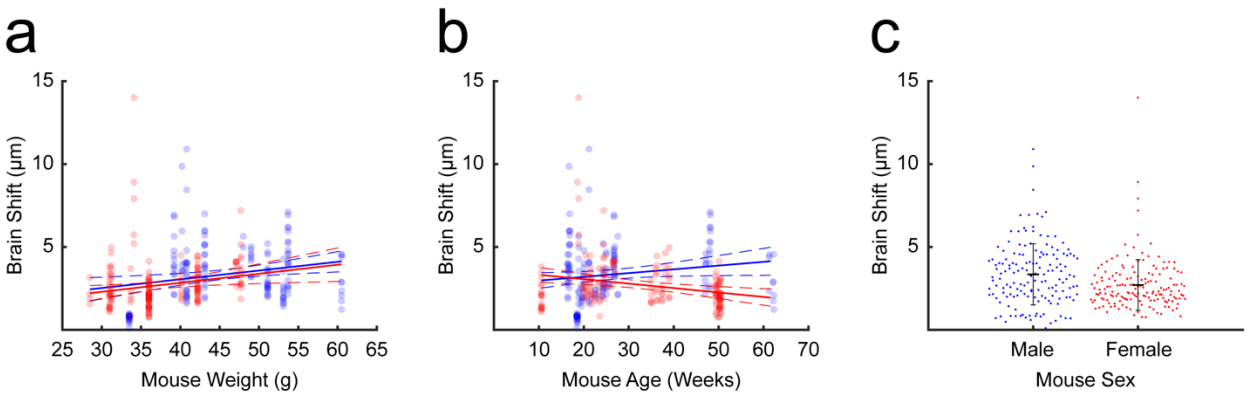

Supplementary Figure 3. The impacts of sex, age, and weight on measured brain motion. a. Magnitude of brain displacement within the skull plotted as a function of mouse weight. The solid blue line represents the linear fit for males (N = 154 trials across 68 locations in 12 mice, p = 0.0064, R^2 = 0.0478) and the solid red line represents the linear fit for females (N = 162 trials across 66 locations in 12 mice, p = 0.0145, R^2 = 0.0368). Dashed lines show the 95 percent confidence intervals. **b.** Magnitude of brain displacement within the skull as a function of mouse age. The solid blue line represents the linear fit for males (N = 154 trials across 68 locations in 12 mice, p = 0.0502, R^2 = 0.0250) and the solid red line represents the linear fit for females (N = 162 trials across 66 locations in 12 mice, p = 0.0015, R^2 = 0.0609). Dashed lines show the 95 percent confidence intervals. **c.** Brain displacement for males and females. Bars show the mean and the standard deviation. A two-sample Kolmogorov-Smirnov test on these data sets rejects the null hypothesis that these sets are from the same continuous distribution at a 5 percent significance level (p = 0.00002). N = 154 trials across 68 locations in 12 mice for males and N = 162 trials across 66 locations in 12 mice for females.

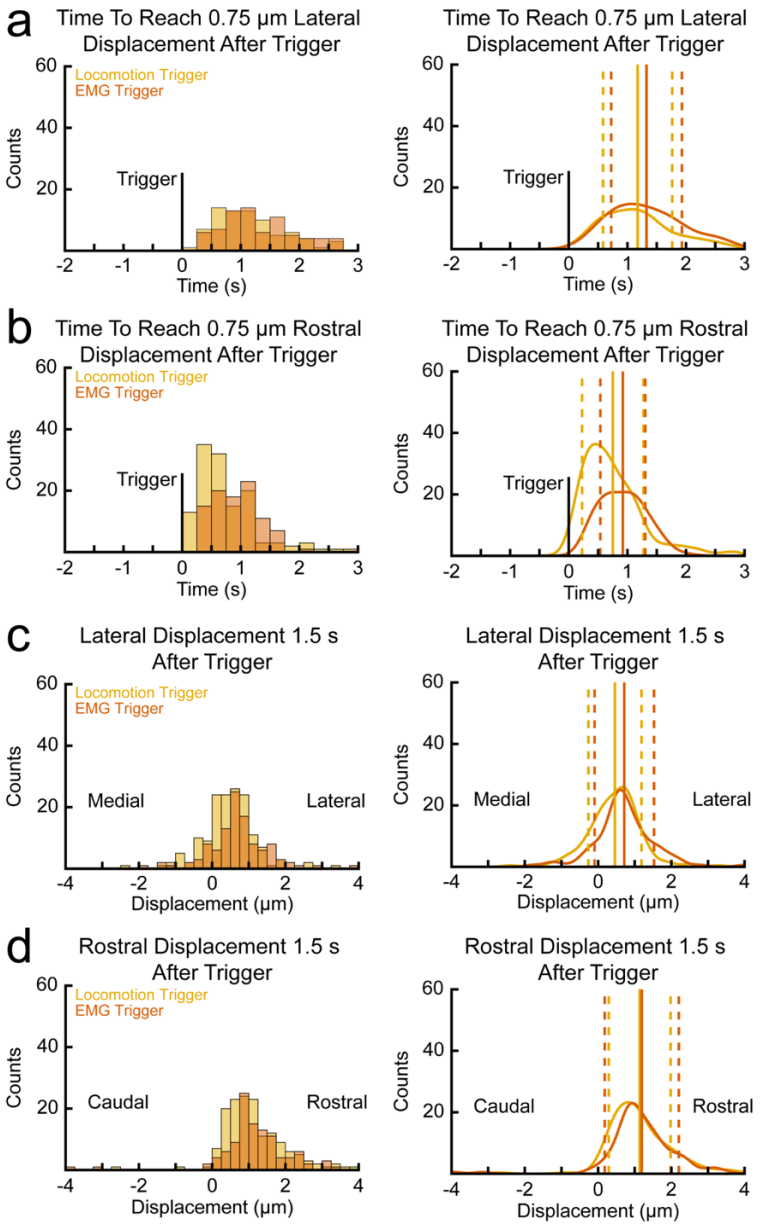

Supplementary Figure 4. The brain displaces with less variability after an electromyography event than a locomotion event. a. The time that the brain takes to displace laterally 0.75µm following a locomotion and EMG event onset as histograms (left) and as probability density functions with corresponding means and standard deviations (right). N=153 locomotion trigger events and N=108 EMG trigger events. **b.** The time that the brain takes to displace rostrally 0.75µm following a locomotion and EMG event onset as histograms (left) and as probability density functions with corresponding means and standard deviations (right). N=153 locomotion trigger events and N=108 EMG trigger events. **c.** The distance the brain has displaced laterally 1.5 seconds after a locomotion and EMG event onset as histograms (left) and as probability density functions with corresponding means and standard deviations (right). N=153 locomotion trigger events and N=108 EMG trigger events. **d.** The distance the brain has displaced rostrally 1.5 seconds after a locomotion (black) and EMG (orange) event onset as histograms (left) and as probability density functions with corresponding means and standard deviations (right). N=153 locomotion trigger events and N=108 EMG trigger events.

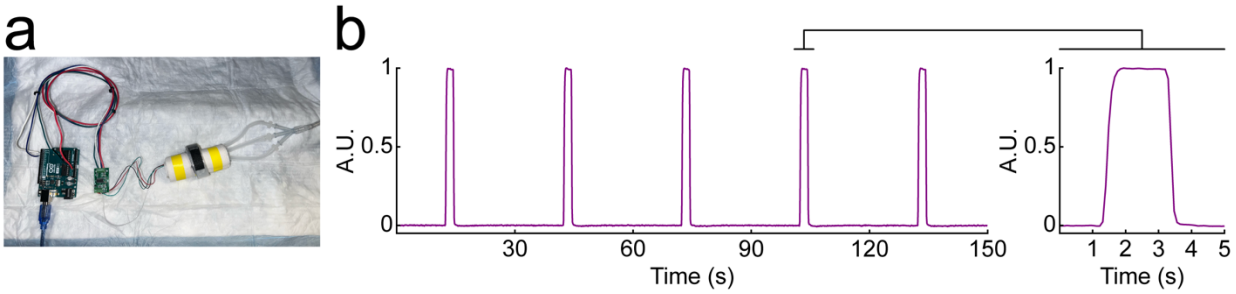

Supplementary Figure 5. Repeatable pressures applied by the inflatable belt. a. An Arduino Uno collected data from a strain gauge wrapped with paper towels and inserted into the inflatable belt used for abdominal compressions. **b.** The belt was inflated with 7 psi of compressed air for two seconds at 30 second intervals. The resulting pressure applied to the strain gauge was consistent in intensity and duration (left). A closer look at a single compression demonstrates the rapid onset and offset transients of the pressure applied (right).

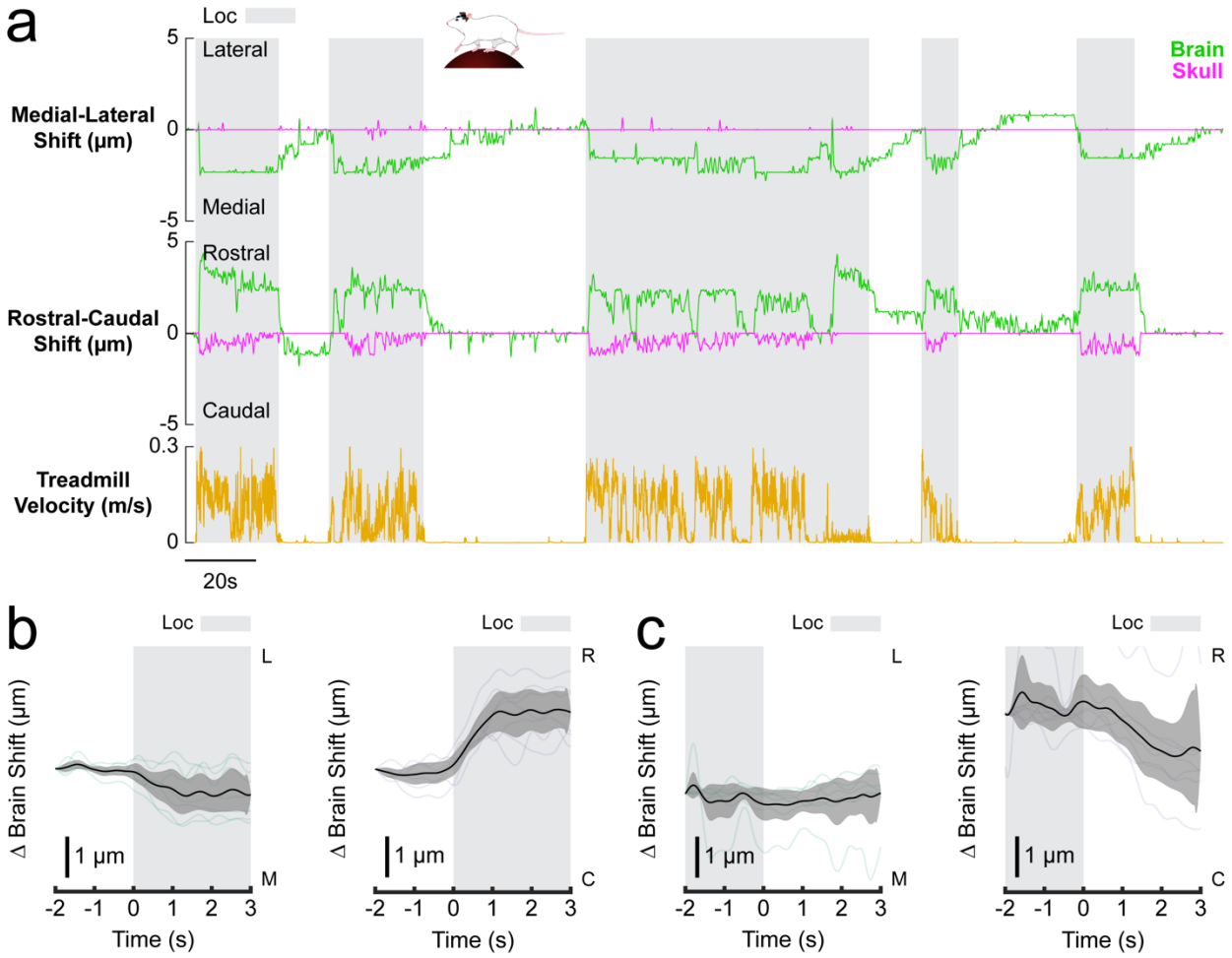

Supplementary Figure 6. Motion of the olfactory bulb was rostral and medial. a. A single trial from an olfactory bulb showing brain (green) and skull (magenta) motion as well as locomotion (orange). Like the cortex, locomotion events resulted in rostral motion of the olfactory bulb. However, the olfactory bulbs exhibited medial displacement instead of lateral. **b.** Locomotion-triggered average olfactory bulb motion for each trial with the average of these plotted in black with the 90 percent confidence interval. N = 7 trials across 5 locations in 3 mice. **c.** Locomotion cessation-triggered average olfactory bulb motion for each trial with the average of these plotted in black with the 90 percent confidence interval. N = 7 trials across 5 locations in 3 mice. Onset and offset of locomotion correspond to t=0.

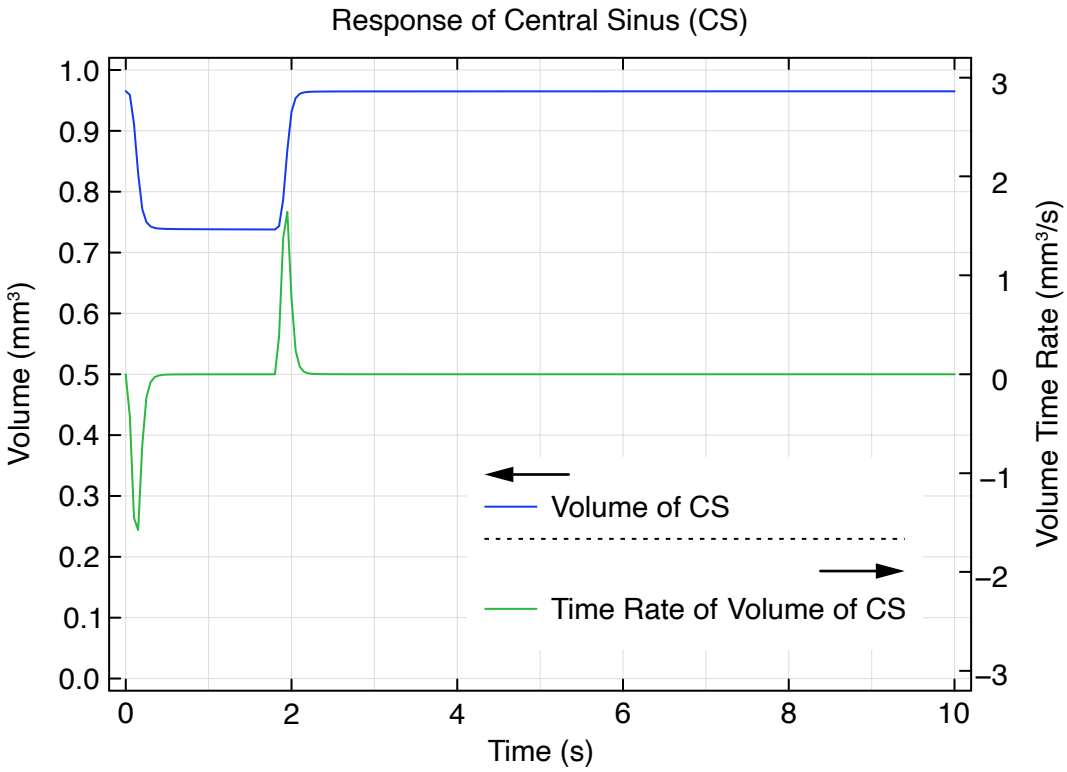

Supplementary Figure 7. Central sinus volume and volume time rate. Volume and time rate of change of volume of the central sinus for the simulation reported in Fig. 6.

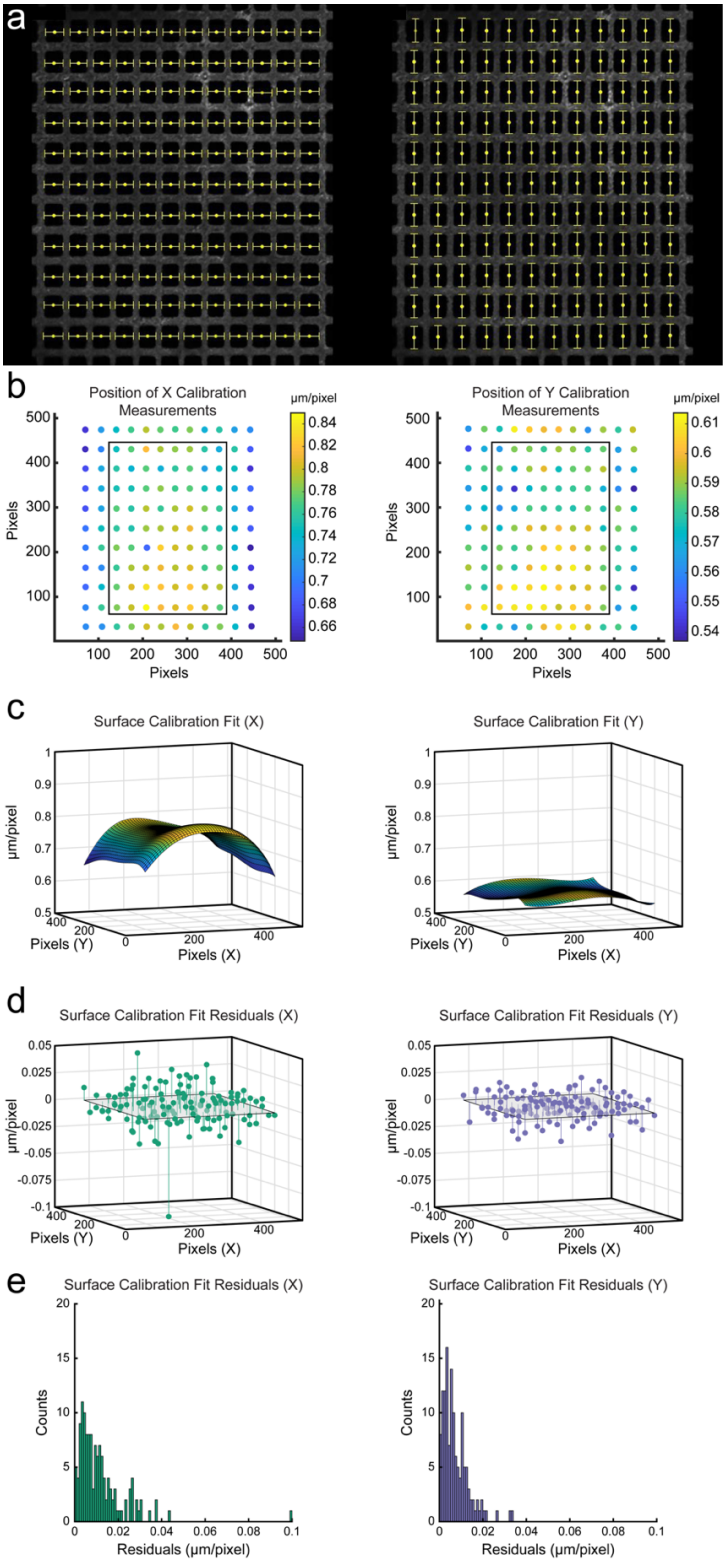

Supplementary Figure 8. Imaging calibration. a. Image of the copper mesh used for calibration. Each 19µm x 19µm hole had its height and width measured in pixels using a full width at half maximum algorithm (yellow bars). **b.** Pixels per micron in the X (left) and Y (right) dimensions. Box shows imaged area. **c.** Fitted surfaces for X (left) and Y (right). **d.** Residuals of the fitted surfaces for X (left) and Y (right). **e.** Histogram representation of the residuals of the fitted surfaces for X (left) and Y (right).

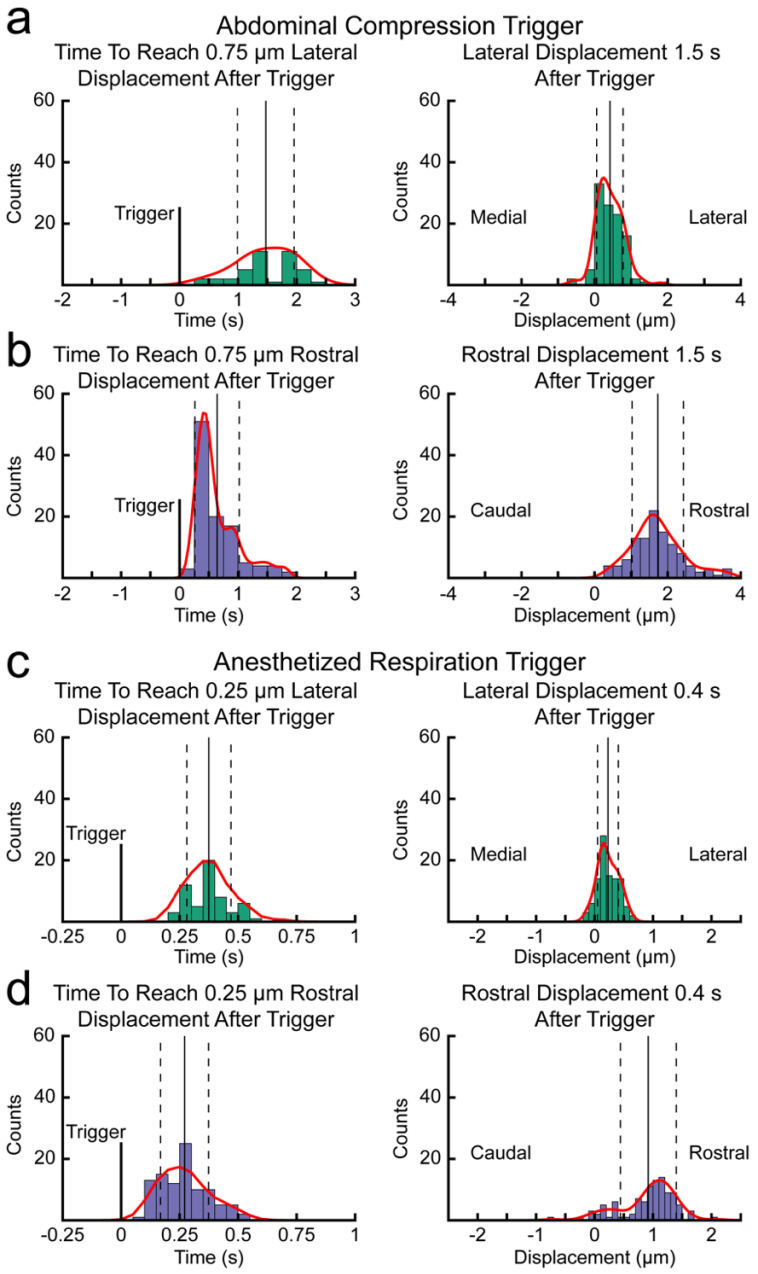

Supplementary Figure 9. Brain displacement speed during externally applied abdominal pressure. a. Histogram of the amount of time it takes the brain to displace laterally 0.75 µm following the onset of an abdominal compression with the probability density function, mean and standard deviation (left). Histogram of lateral displacement of the brain 1.5 seconds following the onset of an abdominal compression with the probability density function, mean and standard deviation (right). N=109 abdominal compression trigger events. **b.** Histogram of the amount of time it takes the brain to rostrally displace 0.75 µm following the onset of an abdominal compression with the probability density function, mean and standard deviation (left). Histogram of rostral displacement of the brain 1.5 seconds following the onset of an abdominal compression with the probability density function, mean and standard deviation (right). N=109 abdominal compression trigger events. **c.** Histogram of the amount of time it takes the brain to displace laterally 0.25 µm following the onset of an anesthetized respiration event with the probability density function, mean and standard deviation (left). Histogram of the lateral displacement of the brain 0.4 seconds following the onset of an anesthetized respiration event with the probability density function, mean and standard deviation (right). N=101 anesthetized respiration trigger events. **d.** Histogram of the amount of time it takes the brain to rostrally displace 0.25 µm following the onset of an anesthetized respiration event with the probability density function, mean and standard deviation (left). Histogram of the rostral displacement of the brain 0.4 seconds following the onset of an anesthetized respiration event with the probability density function, mean and standard deviation (right). N=101 anesthetized respiration trigger events.

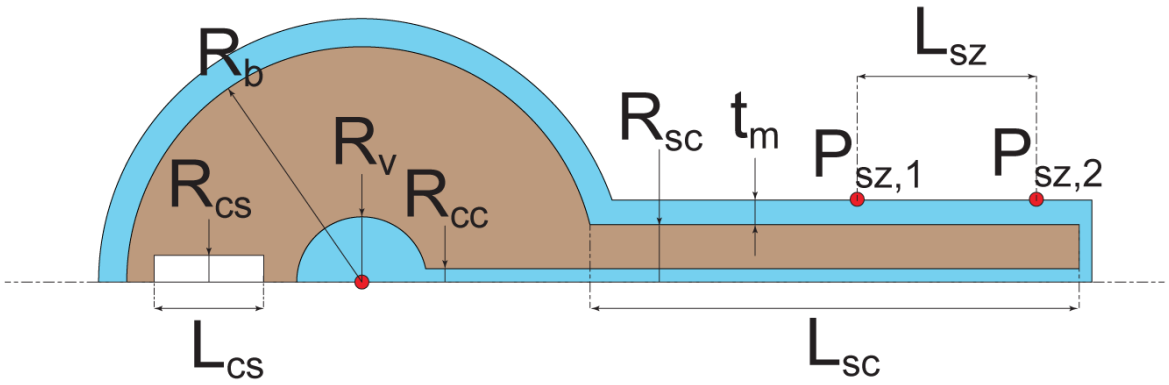

Supplementary Figure 10. Initial geometry (not to scale) of an axially symmetric poroelastic domain (tan) representing brain and spinal cord immersed in CSF-filled poroelastic compartment (cyan), including the cranial and spinal SAS, central canal and a spherical ventricle representing the ventricular system. All geometric parameters defining the model, together with the chosen values are summarized in Table 1. In the geometry implemented in COMSOL Multiphysics for all finite element simulations, corners are rounded using a “fillet” tool.

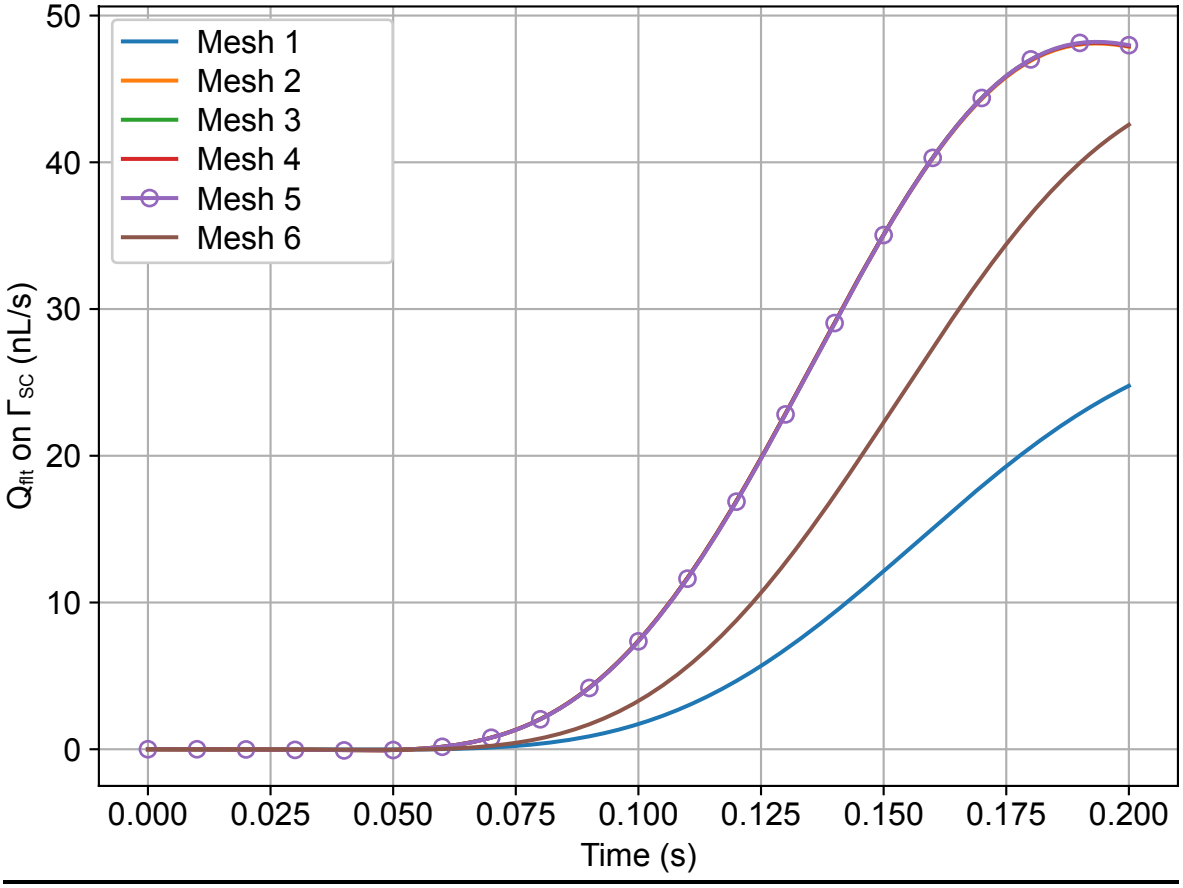

Supplementary Figure 11. Mesh sensitivity study. Flow rate exchange over Γ_{SC} for each of the 6 meshes considered. Mesh 5 is the mesh used in all simulations.

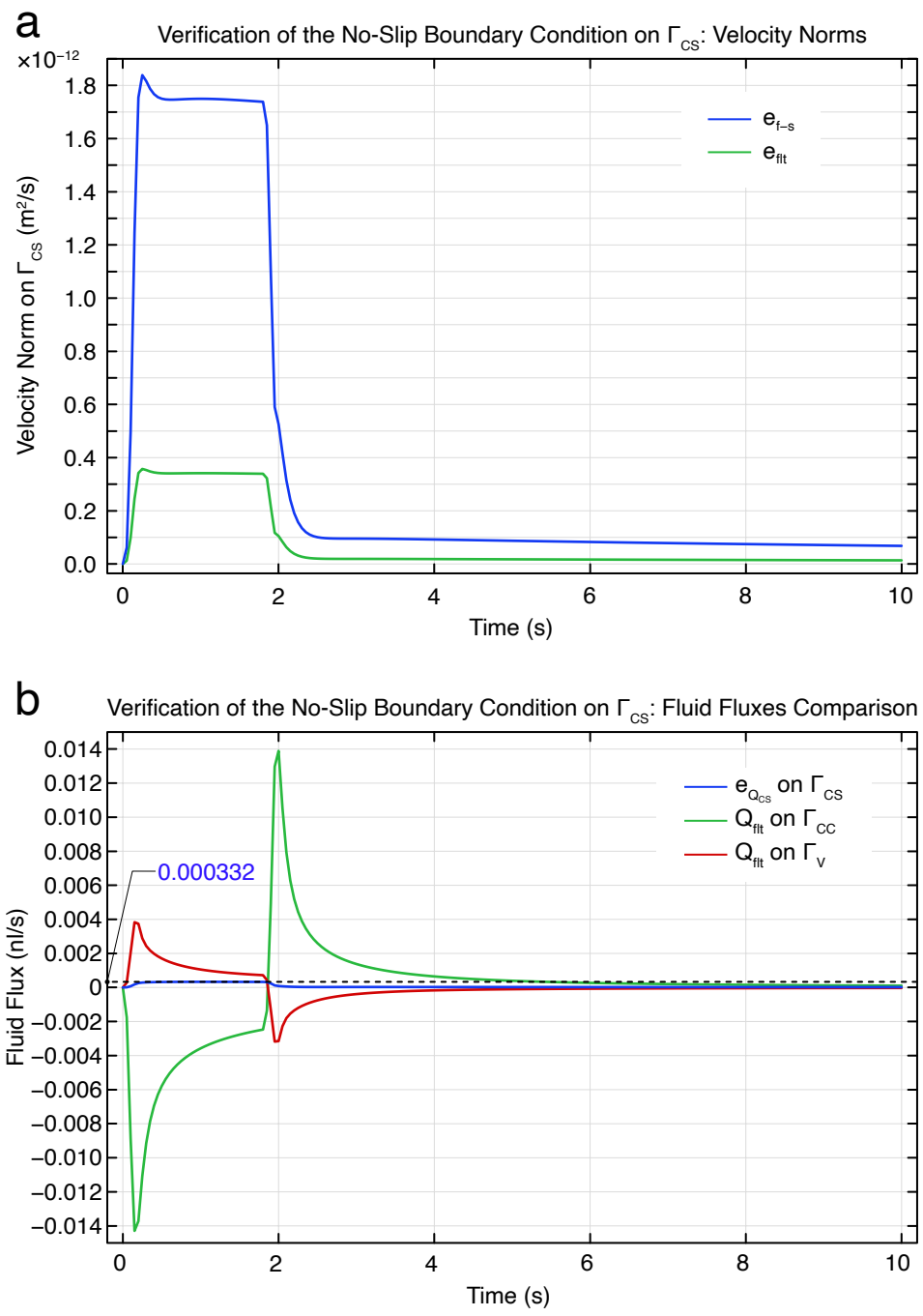

Supplementary Figure 12. Fluid no-slip boundary condition on Γ_{CS} error estimation. a. L^2-norms over Γ_{cs} of the quantity $\boldsymbol{v}_f - \boldsymbol{v}_s$ (line labelled e_{f-s}) and $\boldsymbol{v}_{flt}$ (line labelled e_{flt}) as a function of time. These norms provide an error measure for assessing the accuracy of the weak enforcement of the no-slip boundary condition for the fluid over Γ_{CS}, the surface of the central sinus.

References

1 Kedarasetti, R. T., Drew, P. J. & Costanzo, F. Arterial vasodilation drives convective fluid flow in the brain: a poroelastic model. *Fluids Barriers CNS* **19**, 34 (2022). https://doi.org/10.1186/s12987-022-00326-y

2 Costanzo, F. & Miller, S. T. An Arbitrary Lagrangian--Eulerian Finite Element Formulation for a Poroelasticity Problem Stemming from Mixture Theory. *Computer Methods in Applied Mechanics and Engineering* **323**, 64--97 (2017).

3 Costanzo, F., Jannesari, M. & Ghitti, B. Poroelastic flow across a permeable interface: a Hamilton's principle approach and its finite element implementation. *arxiv* (2025). https://doi.org/10.48550/arXiv.2504.15173

4 dell'Isola, F., Madeo, A. & Seppecher, P. Boundary conditions at fluid-permeable interfaces in porous media: A variational approach. *International Journal of Solids and Structures* **46**, 3150-3164 (2009). https://doi.org/10.1016/j.ijsolstr.2009.04.008

5 Brenner, S. & Scott, L. *The Mathematical Theory of Finite Element Methods*. Vol. 15 (Springer-Verlag, 2008).

6 Bazilevs, Y. & Hughes, T. J. R. Weak imposition of Dirichlet boundary conditions in fluid mechanics. *Computers & Fluids* **36**, 12-26 (2007). https://doi.org/10.1016/j.compfluid.2005.07.012

7 Chung, J. & Hulbert, G. M. A Time Integration Algorithm for Structural Dynamics With Improved Numerical Dissipation: The Generalized-α Method. *Journal of Applied Mechanics* **60**, 371-375 (1993). https://doi.org/10.1115/1.2900803

8 Jansen, K. E., Whiting, C. H. & Hulbert, G. M. A generalized-α method for integrating the filtered Navier–Stokes equations with a stabilized finite element method. *Computer Methods in Applied Mechanics and Engineering* **190**, 305-319 (2000). https://doi.org/10.1016/s0045-7825(00)00203-6